Nanostructure of the laser-modified transition metal nanocomposites for water splitting

OPEN ACCESS
IOP Publishing
Nanotechnology

Nanotechnology **33** (2022) 205401 (8pp)
https://doi.org/10.1088/1361-6528/ac512a

Nanostructure of the laser-modified transition metal nanocomposites for water splitting

Jakub Wawrzyniak[1], Jakub Karczewski[2], Emerson Coy[3], Jacek Ryl[2], Katarzyna Grochowska[1] and Katarzyna Siuzdak[1]

[1] The Szewalski Institute of Fluid-Flow Machinery, Polish Academy of Sciences, Fiszera 14, 80-231 Gdansk, Poland
[2] Faculty of Applied Physics and Mathematics, Institute of Nanotechnology and Materials Engineering, Gdansk University of Technology, Narutowicza 11/12, 80-233 Gdansk, Poland
[3] NanoBioMedical Centre, Adam Mickiewicz University, Wszechnicy Piastowskiej 3, 61-614 Poznan, Poland

E-mail: jwawrzyniak@imp.gda.pl

Received 22 October 2021, revised 13 January 2022
Accepted for publication 2 February 2022
Published 21 February 2022

Abstract

Although hydrogen is considered by many to be the green fuel of the future, nowadays it is primarily produced through steam reforming, which is a process far from ecological. Therefore, emphasis is being put on the development of electrodes capable of the efficient production of hydrogen and oxygen from water. To make the green alternative possible, the solution should be cost-efficient and well processable, generating less waste which is a huge challenge. In this work, the laser-based modification technique of the titania nanotubes containing sputtered transition metal species (Fe, Co, Ni, and Cu) was employed. The characteristics of the electrodes are provided both for the hydrogen and oxygen evolution reactions, where the influence of the laser treatment has been found to have the opposite effect. The structural and chemical analysis of the substrate material provides insight into pathways towards more efficient, low-temperature water splitting. Laser-assisted integration of transition metal with the tubular nanostructure results in the match-like structure where the metal species are accumulated at the head. The electrochemical data indicates a significant decrease in material resistance that leads to an overpotential of only +0.69 V at 10 mA cm^{-2} for nickel-modified material.

Supplementary material for this article is available online

Keywords: laser, titanium dioxide, nanotubes, anodization, water splitting, oxygen evolution

(Some figures may appear in colour only in the online journal)

1. Introduction

The progressing climate change driven by the overuse of fossil deposits compels us to find cleaner, more efficient fuels of the future. Hydrogen is often considered to be one of the best alternatives, due to its incredible energy density, potentially unlimited availability, and, as it burns back to the water, sustainability. Unfortunately, it is rarely created through eco-friendly means, as much cheaper, though dirtier techniques are available. One of the factors contributing to the high price of hydrogen created through electrocatalysis of water is the price of electrode materials, such as platinum group metal species. Similarly, even though high surface area materials are known to perform better catalytically, the techniques used to create them often leave a lot of wasted material during their

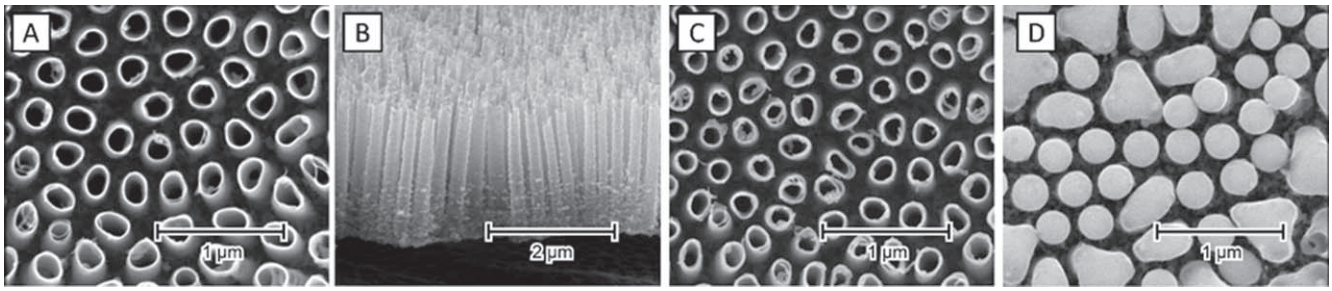

Figure 1. SEM images presenting top (A) and side (B) view of the anodized and calcined titania nanotubes, as well as representative sample of TNTs sputtered with 5 nm nickel layer (C) and treated with laser (D).

synthesis. Moreover, typical wet-chemistry route makes the upscaling difficult and even outstanding results are contained to the laboratory scale. These difficulties incentivize the use of techniques feasible outside laboratory and chemical compounds free of precious elements.

Known for their corrosion resistance, the titania nanotubes (TNTs) with highly developed surface are often synthesized via a scalable electrochemical anodization process [1]. Moreover, through the adjustments in the process parameters, such as electrolyte composition, temperature, and potential applied, their geometry can be tailored, changing their properties depending on the specific needs [2, 3]. Furthermore, due to the bandgap of 3.2 eV the TNTs exhibit photoactive properties in the UV light, which may further improve their catalytic properties under illumination [4]. Although the width of their bandgap hampers their efficiency under the visible light, the TNTs can be regarded as an excellent material for further modification since the nanostructure is already formed onto the stable, conducting substrate which is important for applications in water-splitting devices.

The transition metal oxides, as a part of the non-noble family, are becoming increasingly popular due to vast availability and, thanks to the tailored synthesis pathways, are often almost as feasible as more expensive alternatives [5–10]. The transition metals from the 4th period especially, are one of the most abundant elements on Earth, and although iron, cobalt, nickel, and copper have all been used as catalysts for water splitting, the obtained results vary significantly depending on the synthesis pathways. It is known, however, that the activity of both titania and the transition metal oxides benefits from the presence of defects, such as oxygen vacancies [11–13], therefore, to achieve a simple and efficient synthesis pathway, methods promoting structural disordering should be considered.

We, therefore, propose a titania-based electrode modified with 4th group transition metals (Fe, Co, Ni, Cu) treated with pulsed laser radiation (Nd:YAG, 355 nm) in a vacuum. The proposed approach eliminates the usage of metal liquid precursors, while each fabrication step is already well-controlled on a technological scale. Moreover, the performance of the electrodes towards water splitting in alkaline media is presented, and the reaction overpotential is calculated for the best-performing samples. Furthermore, the selected electrodes underwent a thorough analysis of their morphology (SEM, TEM) as well as optical (UV–vis), physical (Raman, GI-XRD), and electrochemical (voltammetry and impedance spectroscopy) properties, based on which an energy diagram showing possible reaction pathway has been created.

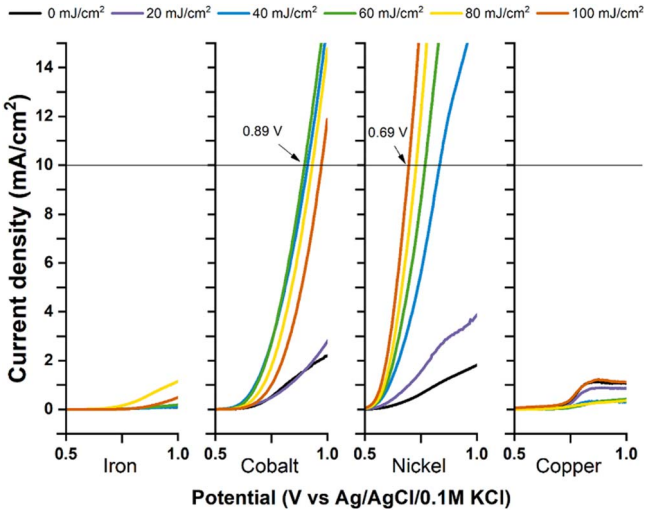

Figure 2. Anodic linear voltammetric sweeps of the Fe, Co, Ni, and Cu-modified titania nanotubes after laser-treatment with 0–100 mJ cm^{-2}.

2. Experimental section

2.1. Synthesis

The titanium foil (99.7% pure, 0.127 mm thick, Strem) was cut into rectangular (20 × 35 mm) pieces which were degreased ultrasonically in acetone (p.a. Protolab), ethanol (96%, Chempur), and deionized water (0.05 μS, Hydrolab). To obtain laterally spaced titania nanotubes, they underwent chemical anodization in a temperature-controlled (40 °C, Julabo F-12) cylindrical cell, where titanium acted as an anode and platinum net (20 × 25 mm) as a cathode. The electrolyte consisted of 0.3 wt% NH4F (Chempur), 0.5 wt% HF (Chempur), and 7 wt% deionized water in diethylene glycol (Chempur). The potential was controlled by in-house built hardware which increased it linearly over 400 s up to 40 V, kept constant for 2 h, and decreased it at the same rate. After the process, the samples were submerged in ethanol for approximately 1 h to wash out the remaining electrolyte. The crystalline, anatase phase was obtained via furnace annealing at 450 °C for 2 h

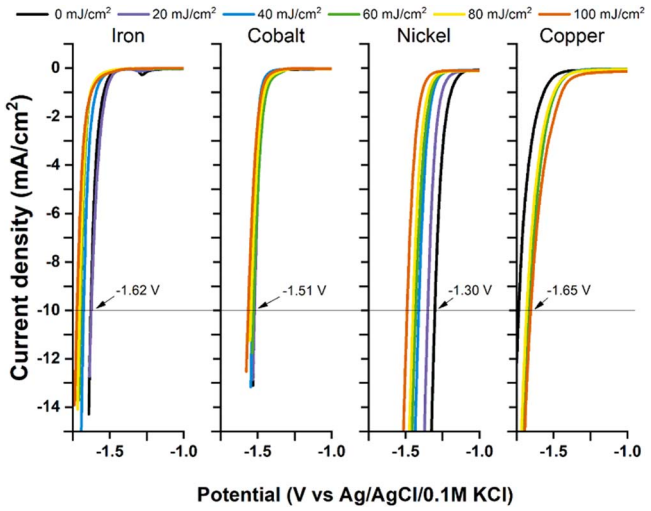

Figure 3. Cathodic linear voltammetric sweeps of the Fe, Co, Ni, and Cu-modified titania nanotubes after laser-treatment with 0–100 mJ cm^{-2}.

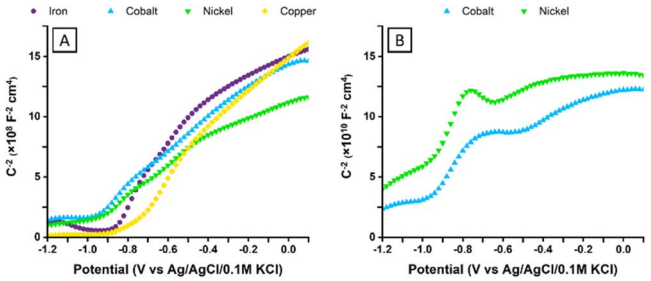

Figure 4. Mott–Schottky diagrams of the modified electrodes in the steady-state (A) as well as Co and Ni electrodes on their first run (B).

(Nabertherm), where the heating rate was set to 2 °C min^{-1}. The samples were sputtered (Quorum Technologies, Q150T S) with 5 nm of iron (Micro to Nano), cobalt, nickel, and copper (Quorum Technologies) and treated with 355 nm laser pulses (Quantel, Nd:YAG, 3ω) in a vacuum (<5 × 10^{-8} bar, Pfeiffer) with fluence in the range of 0–100 mJ cm^{-2}.

2.2. Characterization

The scanning electron microscope (SEM) images were taken by FE-SEM FEI Quanta FEG 250, whereas transmission electron microscope (TEM) pictures were done using JEOL ARM 200F (200 eV) equipped with an energy-dispersive x-ray spectrometer (EDX). The grazing incidence x-ray diffraction patterns (GI-XRD) were obtained via PANalytical X'pert MRD diffractometer with Kα radiation, operating at 45 mA and 40 kV. The dual-beam UV–vis spectrometer (Lambda 35, Perkin-Elmer) equipped with diffuse reflectance accessory was used to obtain reflectance UV–vis spectra, whereas a confocal Raman spectrometer (InVia Renishaw) equipped with a 514 nm laser and a ×50 lens was used to extract the Raman spectra. The x-ray photoelectron spectra (XPS) were obtained via Escalab250Xi calibrated for adventitious C1s (284.6 eV) [14]. The electrochemical performance of the samples was determined using Autolab PGStat 302 N potentiostat-galvanostat in a three-electrode system, where the investigated sample was immersed in 0.5 M NaOH electrolyte (Stanlab) and acted as a working electrode whereas Ag/AgCl/0.1 M KCl and platinum mesh were used as a reference- and counter-electrodes respectively. Before the measurements, the electrolyte was deaerated with argon (5 N), while during the test a constant flow of the inert gas above the solution was kept. The simulated solar radiation was provided by Oriel LS0500 equipped with AM 1.5 filter. The radiation intensity was set to 100 mW cm^{-2} and verified using Si reference cell (Rera). The electrochemical cell was equipped with a quartz window transparent to the UV light. The cyclic voltammetry (CV) sweeps in the −0.6 to +0.6 V range at 50 mV s^{-1} were performed before other measurements both in the dark and under illumination ensuring penetration of the electrolyte into the pores of the material. To investigate hydrogen- and oxygen evolution reactions (HER/OER), the polarization was applied from 0 V versus Ag/AgCl/0.1 M KCl at 0.1 mV s^{-1} rate in the anodic and cathodic regions respectively, up to a point where current densities over 10 mA cm^{-2} could be detected. The impedance investigation was conducted in the galvanostatic mode in the dark and under simulated irradiation at current densities of 1 and 10 mA cm^{-2} in the 20 000–1 Hz range at 20 points per decade and amplitude of 10 μA. The Mott–Schottky (MS) analysis was done from +0.1 to −1.2 V at 1 kHz, with 10 mV amplitude. Before recording the impedance data, the electrode was polarized for 15 min and for 1 min between each data point. The charge carrier density was calculated according to the formula [15]

$$N_d = \frac{2}{\varepsilon_0 \varepsilon q}\left[\frac{d\frac{1}{C^2}}{dE}\right]^{-1},$$

where ε_0 is the electric permittivity of vacuum, ε is a relative permittivity of anatase [16], and q stands for the charge of the electron. The expression in the square brackets stands for the slope of the MS plot.

3. Results and discussion

The parameters of the nanotubes were chosen based on previous research [3, 17] to maximize the photoactivity of the substrate material. Figure 1(A) shows the SEM images of the anatase TiO_2 nanotubes from the top, whereas figure 1(B) shows their cross-section. The obtained morphology is characterized by the distinct lateral spacing between the nanotubes (ca. 140 nm), which is only slightly lower than their diameter (ca. 190 nm). Their average wall thickness is 14 nm, and they reach 2 μm in length. The SEM images after sputtering show the thickening of the nanotube rims, as it is where most of the metal is being deposited (figure 1(C)) [18], whereas the representative picture of the laser-treated nanotubes is shown in figure 1(D).

The performance of the prepared electrodes was determined based on their oxygen evolution reaction overpotentials at 10 mA cm^{-2} [19, 20]. The linear voltammetric

Table 1. The values of the flatband potentials and charge carrier densities for the selected samples.

Parameter\Metal	E_{fb} versus Ag/AgCl/0.1 M KCl) (V)	E_{fb} versus RHE (V)	N_d ($\times 10^{19}$ cm^{-3})	N_{di} ($\times 10^{19}$ cm^{-3})
Iron	− 0.87 V	0.22 V	1.14	1.14
Cobalt	− 1.02 V	0.07 V	2.03	0.0136
Nickel	− 1.01 V	0.08 V	2.37	0.0094
Copper	− 0.77 V	0.32 V	1.34	1.30

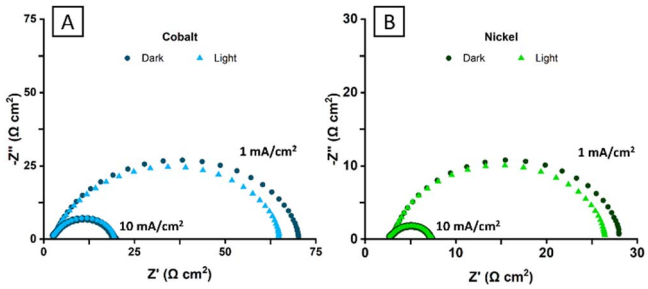

Figure 5. Nyquist representation of the impedance spectra for the electrodes modified with Co and Ni under constant load of 1 and 10 mA cm^{-2} in the dark and under the simulated AM 1.5 illumination.

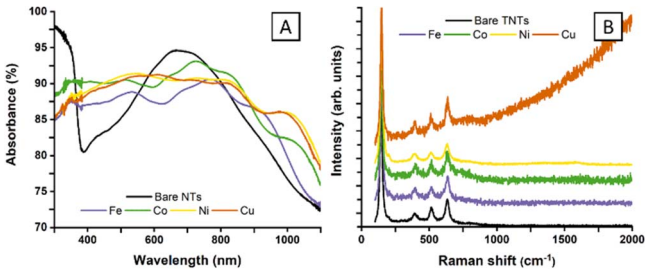

Figure 6. UV–vis absorbance (A) and Raman (B) spectra of the selected samples.

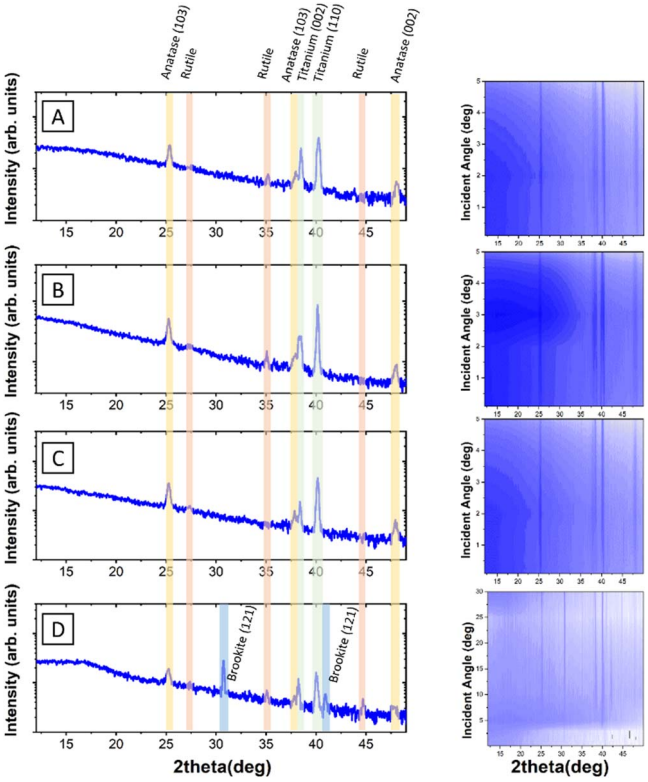

Figure 7. Grazing incidence diffractograms of the electrodes modified with iron (A), cobalt (B), nickel (C), and copper (D).

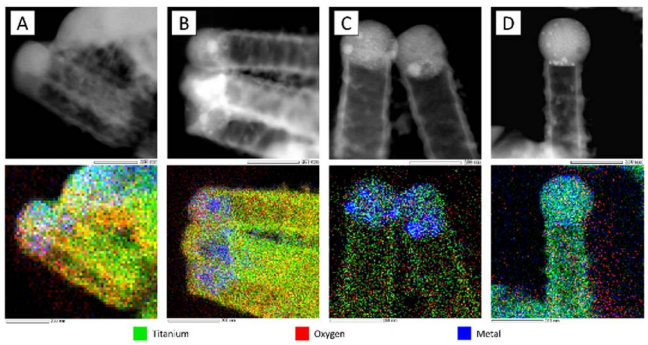

Figure 8. TEM (top) and EDX (bottom) images of the titania nanotubes with 5 nm Fe (A), Co (B), Ni (C), and Cu (D) layer after laser-induced re-solidification of the titania cap.

sweeps in the anodic region for all of the prepared substrates are shown in figure 2. In comparison to the sputtered-only samples, most of the laser-treated specimen exhibit higher current densities in the OER region. In the case of iron-enriched samples, the treatment with 80 mJ cm^{-2} contributed to the highest current density increase, but it only barely passed 1.1 mA cm^{-2} at 1 V. Cobalt, on the other hand, peaked after irradiation with 60 mJ cm^{-2} pulses, reaching 10 mA cm^{-2} at +0.89 V. The most promising results were, however, obtained for electrodes with added nickel and irradiated with 100 mJ cm^{-2}, as the threshold was reached at only +0.69 V. In the case of copper though, the laser treatment had a reverse effect, where treatment with up to 80 mJ cm^{-2} lowered obtained current densities. Irradiation with 100 mJ cm^{-2}, however, had little effect in comparison with the sputtered-only sample. Nonetheless, the samples reached a plateau at +0.85 V at a maximum current density of only 1.2 mA cm^{-2}, not reaching the expected breakpoint of 10 mA cm^{-2}. Interestingly though, the laser treatment resulted in a reverse trend when investigated for hydrogen evolution reaction. Polarization in the cathodic region revealed the lowest overpotentials for sputtered-only samples (0 mJ cm^{-2}) in the case of Fe, Co, and Ni and for Cu irradiated with 100 mJ cm^{-2} (figure 3). The 12 h stability test of the best electrodes show potential change below 3%, indicating good stability under load (ESI (available online at stacks.iop.org/NANO/33/205401/mmedia)). Furthermore, from all of the investigated samples, four best-performing in the OER region (one from each metal) were chosen for further investigation.

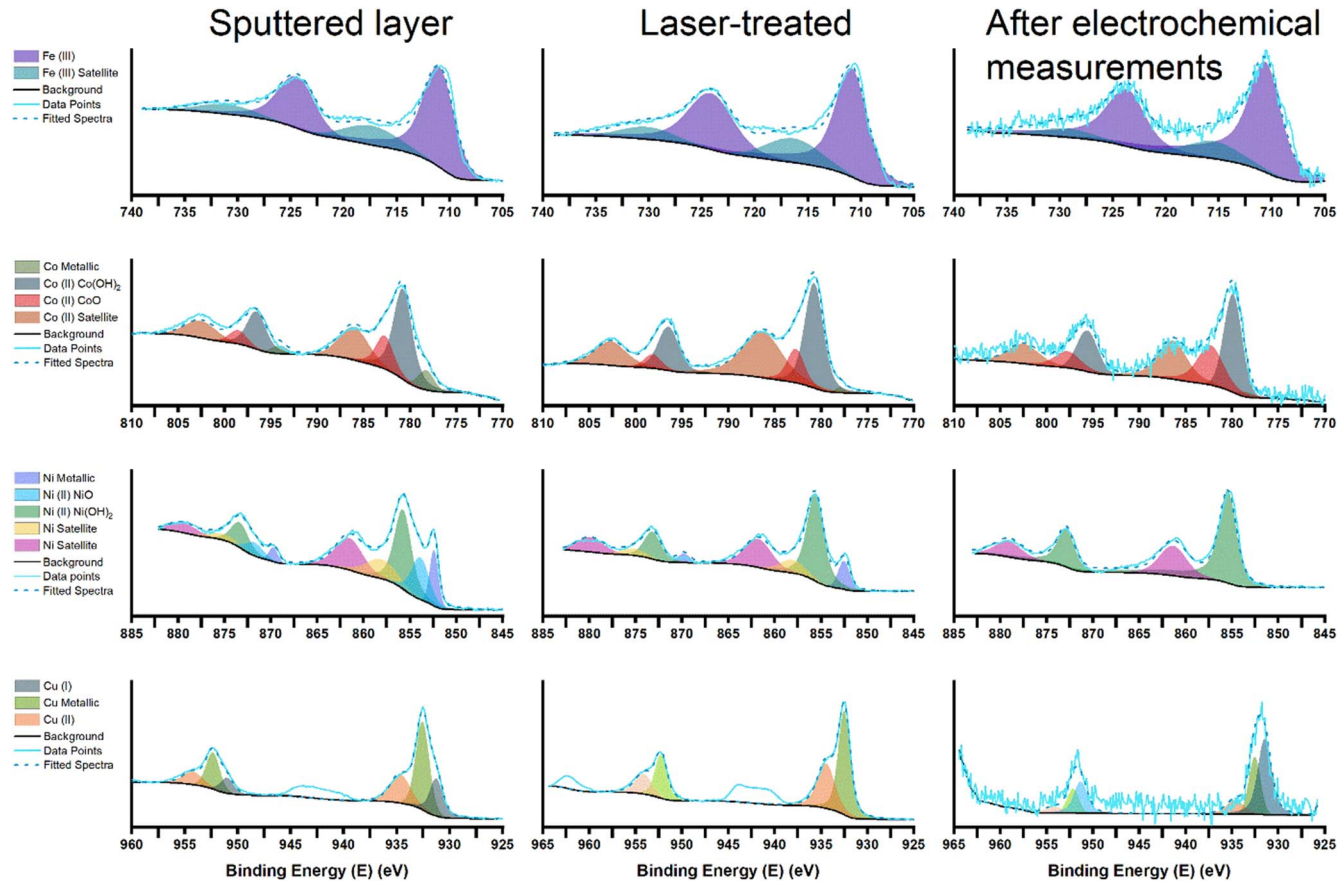

Figure 9. The deconvoluted XPS spectra of the investigated electrodes in their respective metal energy ranges after each modification step.

Although the investigation of the electrodes under AM 1.5 illumination was done alongside the measurements in the dark, the change in overpotential values was within the margin of error (below 0.01 V).

During the investigation, the repeated Mott–Schottky measurements were done, but in the case of nickel- and cobalt-coated electrodes, the initial results varied significantly from the ones obtained in the 2nd and 3rd run. As there should be no reactions occurring on the electrode in the investigated range, this phenomenon was deemed worthy of analysis. Therefore, figure 4(A) presents MS plots for the selected samples in their steady-state (3rd run), whereas figure 4(B) shows the initial run of the Co- and Ni-modified electrodes. It is worth noting, that although the curves obtained from electrodes containing iron and copper did not change their course over three consecutive runs, others underwent a significant transformation which might be attributed to the presence of trap states being filled or oxy-hydroxides formed on the surface [21]. The steady-state flat band potential (E_{fb}) was determined based on the intersection of the tangent to the linear part with the potential axis and subsequently the density of charge carriers (N_d) was calculated from its slope (table 1) [22, 23]. The obtained values show, that the best performing electrodes (Co, Ni) share a similar position of the Fermi level, while the analysis of the slope indicates slightly higher carrier density in a nickel electrode. Both Fe- and Cu-modified substrates exhibit nearly halved charge carrier density and positively shifted E_{fb} levels relative to Ni and Co. Interestingly, the initial number of charge carriers (N_{di}) for the electrodes containing cobalt and nickel was over two orders of magnitude lower.

Based on the performance of the electrodes towards OER (figure 2) and the charge carrier density (table 1), a further electrochemical investigation was done only for the most promising samples. Therefore, figure 5 shows Nyquist representation of the impedance spectra of the samples modified with cobalt and nickel. Although the shapes of the semicircles are very similar in both cases, the values measured in each case differ substantially. Under the 1 mA cm^{-2} load, the semicircles indicate a drop in resistance under simulated solar light in the low-frequency range (∼9% for Co, ∼6% for Ni). However, under an applied load of 10 mA cm^{-2}, the resistance increased by about 1%. Nevertheless, the bulk resistance of the nickel electrode was about 2.5 times lower than for their cobalt counterparts.

The absorbance spectra of the selected specimen are shown in figure 6(A). The reference sample exhibits strong absorption in the UV region, with the cutoff according to its bandgap (3.23 eV), followed by an absorption maximum at ca. 670 nm, most likely from the titanium foil underneath the nanotubes. However, all of the laser-treated samples exhibit decreased UV absorbance due to the creation of oxygen vacancies [24]. On the other hand, despite overall much flatter absorption characteristics, interference fringes are visible

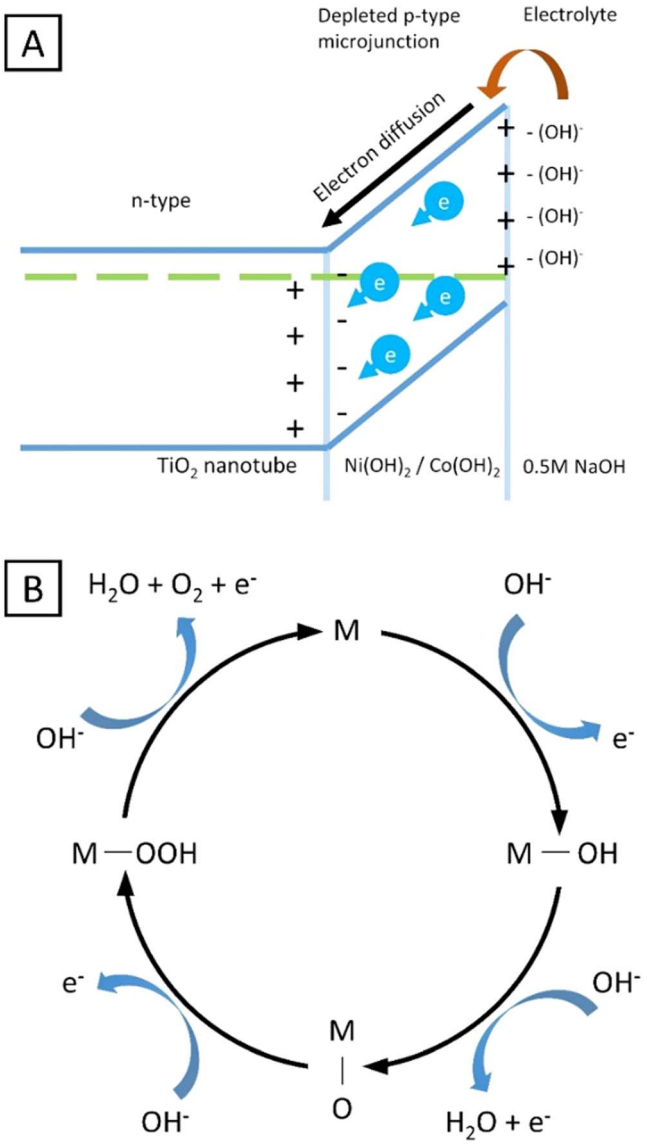

Figure 10. Schematic representation of the micro p-n junction facilitating efficient OER mechanism (A), and the mechanism of oxygen generation through metal oxides in alkaline media (B) [41].

throughout the spectrum. They are caused by the interference of the light reflected from the semi-transparent nanotube seals in their upper region and the titanium sheet underneath. As it is a purely geometrical phenomenon, Chiarello *et al* [25] have proposed an equation, in which the height of the nanotubes can be approximated from the distance of the respective fringes. It is noteworthy, that the two samples modified with 100 mJ cm^{-2} laser pulses (Ni, Cu) show nearly identical absorbance spectrum, proving that the changes in absorbance are driven primarily by the laser irradiation.

The figure 6(B) shows normalized Raman spectra of the investigated samples, with all the peaks expected for anatase: 144 ($E_{g(1)}$), 197 ($E_{g(2)}$), 395 (B_{1g}), 519 (B_{1g}), and 635 ($E_{g(3)}$) cm^{-1} [26], but no signal from any of the metal species. Furthermore, the GI-XRD studies were done to investigate the differences in crystal structure after the laser treatment (figure 7). Despite some artifacts from bending of the sample, contributions from titanium (002), (110) and anatase (101), (103), (002) were found, with a very faint addition of rutile [27]. Interestingly, a relatively strong reflection characteristic to brookite (121) was found in a sample with copper, but neither absorbance, Raman, nor XRD investigation revealed the identifiable presence of metal species on the surface, likely due to their low amount.

The TEM-EDX revealed the distribution of the elements in the modified nanotubes (figure 8). The red color represents the position of oxygen atoms, titanium is marked green, and the sputtered metal is marked blue. Although the Ti and O are distributed evenly through the samples, the Fe, Co, Ni, and Cu are mostly confined to the nanotube cap. The images also indicate, that the nanotube remains empty inside and only the upper part of the nanotube was re-solidified during laser processing, resembling a match head. In the case of cobalt and nickel, the metal is localized in the form of nanoparticles, whereas more uniform distributions of iron and copper within the nanotube can be observed.

Figure 9 shows deconvoluted high-resolution XPS spectra of the electrodes in the energy range of their respective metal which were taken after each modification step. The iron-infused electrode shows Fe (III) contribution at 710.9 with its satellite at 716.6 eV and does not change significantly during the modification process. The cobalt species indicate a small metallic contribution (777.9 eV), cobalt hydroxide (780.7 eV), cobalt oxide (782.7 eV), and the satellite peak (786.5 eV). During the laser- and electrochemical-treatment, the contribution of the metallic cobalt decreases in favor of CoO and $Co(OH)_2$. Similarly, although sample sputtered with nickel shows a strong metallic peak at 852.5 eV, oxide at 853.9 eV, oxyhydroxide at 855.6 eV, and two related satellites at 858.2 and 862.0 eV, the contribution from nickel oxide disappears during the laser-treatment, followed by metallic contribution after electrochemical analysis. In the final electrode, only contributions from nickel oxyhydroxide and its satellite are visible. Lastly, the copper gives a weak Cu_2O signal at 951.0 eV, a strong metallic signal at 932.5 eV, and the Cu (II) at 934.6 with its broad satellite centered at 942.3 eV. Although the Cu (I) transforms into Cu (II) during the laser treatment, the process is reversed when the electrode is polarized in the alkaline electrolyte, which results in Cu (I) being the major factor in the electrode. Interestingly, the Fe, Co, and Cu electrodes exhibit a lower signal-to-noise ratio after measurements in the electrolyte, suggesting that they may dissolve in the electrolyte [28–33]. The two best electrodes (with cobalt and nickel) show similar evolution of the oxidation states, as both of them favor oxyhydroxide creation, which plays an important role in catalytic charge transfer [21, 34, 35]. The progressive hydroxylation of the metallic species in those two electrodes also explains the change of the Mott–Schottky graphs (figure 4(B)), as even though the initial cyclic voltammetric sweeps were performed, the electrodes stabilized only after two impedance sweeps in lower potentials.

Given the results, the mechanism of the charge transfer at the metal-infused titania electrode can be derived (figure 10). Due to the presence of the oxygen vacancies, the anatase TiO_2 is an intrinsic n-type semiconductor [36], the same as iron [37] and copper oxide [38], whereas the CoO, and NiO_2, are

of the p-type [39, 40]. Because the metal species are confined to the uppermost nanotube region (figure 8), we can model the nanotubes sputtered with cobalt and nickel as a p-n junction where, in the steady-state, electrons diffuse from the cap to the nanotube body. The depletion of the cap region accelerates the formation of the double-layer through the binding with hydroxyl groups, which then are transformed into gaseous oxygen. In the alkaline electrolyte, the metal nanoparticles act as trap states for the (OH^-) groups (figure 4(B)), bind with them (figure 9), and act as an efficient channels for charge transport. As the electrodes' performance is dependent on the laser fluence used in modification, it can be responsible for creating additional oxygen vacancies within titania structure. Similarly, exposure to alkaline media facilitates oxidation of the metallic nickel, promoting formation of the p-type layer. As a result of the modification, the potential difference within the depleted micro p-n junction is elevated. Therefore, the same effects are responsible for lowering overpotentials of the oxygen generation and increasing potential required for HER.

4. Conclusions

In this work, the performance of the laser-treated, metal-sputtered titania electrodes towards HER and OER was investigated. Although the irradiation with laser improves the activity towards OER, it has an inverse effect when investigated towards HER (Cu being the exception). The electrochemical and physical investigation allows to conclude, that the improved photocatalytic activity towards OER can be attributed to the micro p-n junction, formed between the nanotube and embedded p-type metal oxides, which allows for easier oxyhydroxide formation on the surface of the electrode. Furthermore, the encapsulation of the nanotubes resulted in an appearance of the interference fringes, which is overall much more uniform than for unmodified material. Although the changes in the impedance spectra indicate photoactivity of the electrodes, illumination with AM 1.5 radiation does not change the obtained overpotential values, which itself appears to be connected to the number of charge carriers present in modified electrodes.

Acknowledgments

This work received financial support from the Polish National Science Centre: Grant No. 2017/26/E/ST5/00416. E.C: Acknowledges the partial financial support from the National Science Centre (NCN) of Poland by the OPUS grant 2019/35/B/ST5/00248.

Data availability statement

All data that support the findings of this study are included within the article (and any supplementary files).

ORCID iDs

Jakub Wawrzyniak https://orcid.org/0000-0001-7664-9584
Jakub Karczewski https://orcid.org/0000-0001-9322-7842
Emerson Coy https://orcid.org/0000-0002-4149-9720
Jacek Ryl https://orcid.org/0000-0002-0247-3851
Katarzyna Grochowska https://orcid.org/0000-0001-7577-3399
Katarzyna Siuzdak https://orcid.org/0000-0001-7434-6408

References

[1] Xiang C, Sun L, Wang Y, Wang G, Zhao X and Zhang S 2017 Large-scale, uniform, and superhydrophobic titania nanotubes at the inner surface of 1000 mm long titanium tubes *J. Phys. Chem.* C **121** 15448–55
[2] Ozkan S, Nguyen N T, Mazare A and Schmuki P 2018 Optimized spacing between TiO_2 nanotubes for enhanced light harvesting and charge transfer *ChemElectroChem* **5** 3183–90
[3] Wawrzyniak J, Grochowska K, Karczewski J, Kupracz P, Ryl J, Dołęga A and Siuzdak K 2020 The geometry of free-standing titania nanotubes as a critical factor controlling their optical and photoelectrochemical performance *Surf. Coat. Technol.* **389** 125628
[4] Wawrzyniak J, Karczewski J, Coy E, Iatsunskyi I, Ryl J, Gazda M, Grochowska K and Siuzdak K 2021 Spectacular oxygen evolution reaction enhancement through laser processing of the nickel-decorated titania nanotubes *Adv. Mater. Interfaces* **8** 2001420
[5] Wang Z, Zhang L, Schülli T U, Bai Y, Monny S A, Du A and Wang L 2019 Identifying copper vacancies and their role in the CuO based photocathode for water splitting *Angew. Chem. Int. Ed.* **58** 17604–9
[6] Wang J, Cui W, Liu Q, Xing Z, Asiri A M and Sun X 2016 Recent progress in cobalt-based heterogeneous catalysts for electrochemical water splitting *Adv. Mater.* **28** 215–30
[7] Jang J-W *et al* 2015 Enabling unassisted solar water splitting by iron oxide and silicon *Nat. Commun.* **6** 7447
[8] Artero V, Chavarot-Kerlidou M and Fontecave M 2011 Splitting water with cobalt *Angew. Chem. Int. Ed.* **50** 7238–66
[9] Tsai H-C, Vedhanarayanan B and Lin T-W 2019 Freestanding and hierarchically structured au-dendrites/3D-graphene scaffold supports highly active and stable Ni_3S_2 electrocatalyst toward overall water splitting *ACS Appl. Energy Mater.* **2** 3708–16
[10] Vedhanarayanan B, Shi J, Lin J-Y, Yun S and Lin T-W 2021 Enhanced activity and stability of MoS_2 through enriching 1T-phase by covalent functionalization for energy conversion applications *Chem. Eng. J.* **403** 126318
[11] Domaschke M, Zhou X, Wergen L, Romeis S, Miehlich M E, Meyer K, Peukert W and Schmuki P 2019 Magnéli-phases in anatase strongly promote cocatalyst-free photocatalytic hydrogen evolution *ACS Catal.* **9** 3627–32
[12] Wang Y, Liang Z, Zheng H and Cao R 2020 Recent progress on defect-rich transition metal oxides and their energy-related applications *Chem.—Asian J.* **15** 3717–36
[13] Xiong X *et al* 2018 A highly-efficient oxygen evolution electrode based on defective nickel-iron layered double hydroxide *Sci. China Mater.* **61** 939–47
[14] Swift P 1982 Adventitious carbon?The panacea for energy referencing? *Surf. Interface Anal.* **4** 47–51

[15] Haryński Ł, Grochowska K, Karczewski J, Ryl J and Siuzdak K 2020 Scalable route toward superior photoresponse of UV-laser-treated TiO_2 nanotubes *ACS Appl. Mater. Interfaces* **12** 3225–35
[16] Park B H, Li L S, Gibbons B J, Huang J Y and Jia Q X 2001 Photovoltaic response and dielectric properties of epitaxial anatase-TiO_2 films grown on conductive $La_{0.5}Sr_{0.5}CoO_3$ electrodes *Appl. Phys. Lett.* **79** 2797–9
[17] Ozkan S, Mazare A and Schmuki P 2018 Critical parameters and factors in the formation of spaced TiO_2 nanotubes by self-organizing anodization *Electrochim. Acta* **268** 435–47
[18] Grochowska K, Ryl J, Karczewski J, Śliwiński G, Cenian A and Siuzdak K 2019 Non-enzymatic flexible glucose sensing platform based on nanostructured TiO_2–Au composite *J. Electroanal. Chem.* **837** 230–9
[19] McCrory C C L, Jung S, Peters J C and Jaramillo T F 2013 Benchmarking heterogeneous electrocatalysts for the oxygen evolution reaction *J. Am. Chem. Soc.* **135** 16977–87
[20] Weber M F and Dignam M J 1984 Efficiency of splitting water with semiconducting photoelectrodes *J. Electrochem. Soc.* **131** 1258–65
[21] Xu Z J 2020 Transition metal oxides for water oxidation: all about oxyhydroxides? *Sci. China Mater.* **63** 3–7
[22] Beranek R 2011 (Photo)electrochemical methods for the determination of the band edge positions of TiO_2-based nanomaterials *Adv. Phys. Chem.* **2011** 1–20
[23] Tsuchiya H, Macak J M, Ghicov A, Räder A S, Taveira L and Schmuki P 2007 Characterization of electronic properties of TiO_2 nanotube films *Corros. Sci.* **49** 203–10
[24] Pasikhani J V, Gilani N and Pirbazari A E 2018 Improvement the wastewater purification by TiO_2 nanotube arrays: the effect of etching-step on the photo-generated charge carriers and photocatalytic activity of anodic TiO_2 nanotubes *Solid State Sci.* **84** 57–74
[25] Chiarello G L, Zuliani A, Ceresoli D, Martinazzo R and Selli E 2016 Exploiting the photonic crystal properties of TiO_2 nanotube arrays to enhance photocatalytic hydrogen production *ACS Catal.* **6** 1345–53
[26] Chen X and Mao S S 2007 Titanium dioxide nanomaterials: synthesis, properties, modifications, and applications *Chem. Rev.* **107** 2891–959
[27] Haryński Ł, Grochowska K, Kupracz P, Karczewski J, Coy E and Siuzdak K 2020 The in-depth studies of pulsed UV laser-modified TiO_2 nanotubes: the influence of geometry, crystallinity, and processing parameters *Nanomaterials* **10** 430
[28] Uhlig I, Szargan R, Nesbitt H W and Laajalehto K 2001 Surface states and reactivity of pyrite and marcasite *Appl. Surf. Sci.* **179** 222–9
[29] Biesinger M C, Payne B P, Grosvenor A P, Lau L W M, Gerson A R and Smart R S C 2011 Resolving surface chemical states in XPS analysis of first row transition metals, oxides and hydroxides: Cr, Mn, Fe, Co and Ni *Appl. Surf. Sci.* **257** 2717–30
[30] Graat P C J and Somers M A J 1996 Simultaneous determination of composition and thickness of thin iron-oxide films from XPS Fe 2p spectra *Appl. Surf. Sci.* **100–101** 36–40
[31] Wu C-K, Yin M, O'Brien S and Koberstein J T 2006 Quantitative analysis of copper oxide nanoparticle composition and structure by x-ray photoelectron spectroscopy *Chem. Mater.* **18** 6054–8
[32] Khan M A, Nayan N, Shadiullah S, Ahmad M K and Soon C F 2020 Surface study of CuO nanopetals by advanced nanocharacterization techniques with enhanced optical and catalytic properties *Nanomaterials* **10** 1298
[33] Pourbaix M 1974 *Atlas of Electrochemical Equilibria in Aqueous Solutions* (Houston, Texas: National Association of Corrosion Engineers (NACE))
[34] Dionigi F *et al* 2020 *In-situ* structure and catalytic mechanism of NiFe and CoFe layered double hydroxides during oxygen evolution *Nat. Commun.* **11** 2522
[35] Chen T-Y, Vedhanarayanan B, Lin S-Y, Shao L-D, Sofer Z, Lin J-Y and Lin T-W 2020 Electrodeposited NiSe on a forest of carbon nanotubes as a free-standing electrode for hybrid supercapacitors and overall water splitting *J. Colloid Interface Sci.* **574** 300–11
[36] Coronado J M and Hernández-Alonso M D 2013 The keys of success: TiO_2 as a benchmark photocatalyst *Design of Advanced Photocatalytic Materials for Energy and Environmental Applications* ed J M Coronado *et al* (London: Springer London) pp 85–101
[37] Kobayashi S and Ichimura M 2018 Electrochemical deposition of Cu-doped p-type iron oxide thin films *Semicond. Sci. Technol.* **33** 105006
[38] Xiong L, Huang S, Yang X, Qiu M, Chen Z and Yu Y 2011 p-type and n-type Cu_2O semiconductor thin films: controllable preparation by simple solvothermal method and photoelectrochemical properties *Electrochim. Acta* **56** 2735–9
[39] Vladimirova S, Krivetskiy V, Rumyantseva M, Gaskov A, Mordvinova N, Lebedev O, Martyshov M and Forsh P 2017 Co_3O_4 as p-type material for CO sensing in humid air *Sensors* **17** 2216
[40] Irwin M D, Buchholz D B, Hains A W, Chang R P H and Marks T J 2008 p-type semiconducting nickel oxide as an efficiency-enhancing anode interfacial layer in polymer bulk-heterojunction solar cells *Proc. Natl Acad. Sci.* **105** 2783–7
[41] Yan Z, Liu H, Hao Z, Yu M, Chen X and Chen J 2020 Electrodeposition of (hydro)oxides for an oxygen evolution electrode *Chem. Sci.* **11** 10614–25